remote sensing

MDPI

Article

Improving Performance of Uncombined PPP-AR Model with Ambiguity Constraints

Yichen Liu [1,2,*], **Urs Hugentobler** [1] **and Bingbing Duan** [1]

[1] Institute for Astronomical and Physical Geodesy, Technical University of Munich, 80333 Munich, Germany; urs.hugentobler@tum.de (U.H.); bingbing.duan@tum.de (B.D.)
[2] Bosch Research, 31139 Hildesheim, Germany
* Correspondence: yichen.liu@tum.de

Abstract: With the advancement of multi-frequency and multi-constellation GNSS signals and the introduction of observable-specific bias (OSB) products, the uncombined precise point positioning (PPP) model has grown more prevalent. However, this model faces challenges due to the large number of estimated parameters, resulting in strong correlations between state parameters, such as clock errors, ionospheric delays, and hardware biases. This can slow down the convergence time and impede ambiguity resolution. We propose two methods to improve the triple-frequency uncombined PPP-AR model by integrating ambiguity constraints. The first approach makes use of the resolved ambiguities from dual-frequency ionosphere-free combined PPP-AR processing and incorporates them as constraints into triple-frequency uncombined PPP-AR processing. While this approach requires the implementation of two filters, increasing computational demands and thereby limiting its feasibility for real-time applications, it effectively reduces parameter correlations and facilitates ambiguity resolution in post-processing. The second approach incorporates fixed extra-wide-lane (EWL) and wide-lane (WL) ambiguities directly, allowing for rapid convergence, and is well suited for real-time processing. Results show that, compared to the uncombined PPP-AR model, integrating N1 and N2 constraints reduces averaged convergence time from 8.2 to 6.4 min horizontally and 13.9 to 10.7 min vertically in the float solution. On the other hand, integrating EWL and WL ambiguity constraints reduces the horizontal convergence to 5.9 min in the float solution and to 4.6 min for horizontal and 9.7 min for vertical convergence in the fixed solution. Both methods significantly enhance the ambiguity resolution in the uncombined triple-frequency PPP model, increasing the validated fixing rate from approximately 80% to 89%.

Keywords: precise point positioning; ambiguity resolution; ambiguity constraints; PPP-AR

check for updates

Citation: Liu, Y.; Hugentobler, U.; Duan, B. Improving Performance of Uncombined PPP-AR Model with Ambiguity Constraints. *Remote Sens.* **2024**, *16*, 4537. https://doi.org/10.3390/rs16234537

Academic Editors: Baocheng Zhang and Yunbin Yuan

Received: 2 October 2024
Revised: 23 November 2024
Accepted: 24 November 2024
Published: 3 December 2024

1. Introduction

Precise Point Positioning (PPP) leverages precise corrections for satellite orbit and clock errors to achieve centimeter- or even sub-centimeter-level positioning accuracy [1,2]. Despite its global coverage and flexibility, PPP suffers from long convergence time, e.g., tens of minutes. To address this challenge, extensive research has focused on improving the convergence and initialization processes of PPP [3–7]. With the development of the global navigation satellite system (GNSS), it comes naturally to use multi-frequency multi-constellation signals jointly. In multi-frequency data processing, uncombined processing of raw observations has gained popularity as it reduces the complexity of forming linear combinations and fully exploits the information contained in each raw observation [8–10]. As opposed to the combined model that utilizes ionosphere-free (IF) combinations for code and phase independently, i.e., implicitly estimating the ionosphere delay parameter without considering that the ionosphere delay is the same for both measurement types for a given satellite, the uncombined model estimates explicitly one common slant ionosphere parameter for each satellite, which in principle leads to a higher degree of freedom [11].

The uncombined model faces challenges due to the increased number of estimated parameters, resulting in high correlations between the state parameters, particularly between the clock errors, ionosphere delays, and hardware biases. Such correlations can slow down the convergence time and hinder the ambiguities from getting resolved. One way to shorten the convergence time in the uncombined model is to apply atmospheric corrections and constrain the corresponding parameters. Aggrey [12] showed that using Global Ionospheric Maps (GIMs) and tropospheric zenith path delays improves PPP initialization. Zhang et al. [13] demonstrated that ionospheric delays derived from regional dense networks are more precise than GIMs, reducing the convergence time from 16 min to 11 min. However, this method needs infrastructure to generate and broadcast local atmospheric corrections. For users to achieve optimal solutions, it is crucial to know the uncertainty of these corrections, which is often not provided.

Another well-established way to improve PPP convergence time and accuracy is to optimize through ambiguity resolution (AR). Three main network models are utilized to provide corrections to enable PPP-AR: the fractional cycle bias (FCB) model [14], the integer recovery clock (IRC) model [15], and the decoupled clock model (DCM) [16]. While the analysis centers (ACs) of the International GNSS Service (IGS) provide dedicated products, the IGS PPP-AR working group also provides the combination of PPP-AR products derived from different ACs [17]. For triple frequency ambiguity resolution, TCAR (Three-Carrier Ambiguity Resolution) and CIR (Cascading Integer Resolution) were proposed [18,19]. TCAR/CIR resolves ambiguities sequentially, starting with the extra-wide-lane (EWL) combination, followed by the wide-lane (WL) combination, and finally the narrow-lane (NL) combination. Many studies have investigated TCAR/CIR within the context of the PPP ionosphere-free combined model [20–22]. In previous research, EWL, WL, and NL ambiguities were typically resolved sequentially to obtain a fixed solution. However, there has been limited investigation into the integration of these ambiguities directly within the filtering process to assess potential improvements in performance. In recent years, the introduction of observable-specific signal biases (OSBs), which provide bias corrections for each pseudorange and phase measurement across all tracking channels, has enabled users to apply satellite signal biases directly to raw GNSS observables [23,24]. This enhances the flexibility and convenience of PPP-AR of any frequency choices at the user end while also making the uncombined model more appealing. Liu et al. [25] derived GPS OSBs using MGEX stations and assessed the performance of triple-frequency PPP-AR with GPS-only observations. Li et al. [26] evaluated the performance of combined and uncombined PPP-AR models with BDS/GPS/Galileo signals but limited their analysis to dual-frequency configurations.

There is still scope for the improvement of PPP-AR using triple-frequency signals. Duan et al. [27] evaluated the quality of Galileo satellite products derived from dual-frequency and multi-frequency measurements, where the fixed integer ambiguities of E1 and E5a in the dual-frequency IF combined PPP model are introduced into uncombined multi-frequency phase equations to reduce the correlation between the parameters. Inspired by this, our study aims to enhance the performance of the triple-frequency uncombined PPP-AR model by integrating ambiguity constraints from two sources: (1) the fixed ambiguities from dual-frequency IF combined PPP model and (2) EWL and WL ambiguities derived from Hatch–Melbourne–Wübbena (HMW) linear combination [28–30]. We focus on how different ambiguity constraints benefit PPP performance, intending to improve convergence speed and ensure reliable ambiguity resolution. To conduct a comprehensive comparative analysis, we process both dual-frequency and triple-frequency signals simultaneously from the GPS and Galileo constellations.

The remainder of this work is structured as follows: after the introduction, the methodology of this study is described in Section 2. Section 3 outlines the data and processing strategy. The results are analyzed and discussed in Section 4. This paper ends with the conclusion and future work in Section 5.

2. Methodology

This section provides a concise overview of the classical PPP models and introduces two new models that incorporate ambiguity constraints. For clarity, the models included are summarized in Table 1. It is important to note that GPS Block IIR and Block IIR-M satellites transmit only L1 and L2 signals. The triple-frequency processing in this study thus adopts a mixed approach, where dual- and triple-frequency measurements are processed together for GPS satellites, while triple-frequency measurements are processed for Galileo satellites.

Table 1. PPP models implemented in this study.

Model	Description
Dual-IF	Dual-frequency measurements with IF combination
Triple-TCAR	Triple-frequency measurements with IF combination
Triple-Uncomb	Raw triple-frequency measurements
Triple-Uncomb+N1&N2	Raw triple-frequency measurements with N1 and N2 ambiguity constraints
Triple-Uncomb+EWL&WL	Raw triple-frequency measurements with EWL and WL ambiguity constraints

2.1. *Classical PPP Models*

Throughout the study, the following equations are used to represent the raw pseudorange measurement P and carrier phase measurement L on frequency i $(i = 1, 2, 3)$ considering the receiver r and satellite s :

$$\begin{aligned} P^s_{r,i} &= \rho^s_r + c(dt_r - dt^s) + \gamma_i I^s_{r,1} + M^s_r T_r + b_{r,i} - b^s_i + \epsilon_{P_i} \\ L^s_{r,i} &= \rho^s_r + c(dt_r - dt^s) - \gamma_i I^s_{r,1} + M^s_r T_r + \lambda_i (N^s_{r,i} + B_{r,i} - B^s_i) + \epsilon_{L_i} \end{aligned} \tag{1}$$

where ρ^s_r represents the geometric distance between receiver r and satellite s, c is the speed of light in vacuum. dt_r and dt^s denote the receiver clock and satellite clock errors, respectively. $\gamma_i = \frac{f_1^2}{f_i^2}$ is the frequency ratio to convert the first-frequency slant ionospheric delay $I^s_{r,1}$ to the ionospheric delay at frequency i. M^s_r refers to the mapping function used to map the zenith troposphere delay T_r to line-of-sight troposphere delay between satellite s and receiver r. λ_i denotes the carrier phase wavelength, $N^s_{r,i}$ is the integer ambiguity on frequency i. $b_{r,i}$ and b^s_i are the receiver-dependent and satellite-dependent hardware code biases. $B_{r,i}$ and B^s_i are the hardware phase biases sourced from the receiver and satellite, respectively. ϵ_{P_i} and ϵ_{L_i} are the unmodeled error terms for pseudorange and carrier phase measurements, respectively, including multipath, higher-order ionospheric effects, measurement noise, etc.

2.1.1. Dual-IF Model

The conventional dual-frequency PPP model makes use of IF combination for code and phase measurement to get rid of first-order ionosphere delay. For simplicity, the satellite clock errors and biases are omitted in the equation as they are corrected using dedicated satellite products, e.g., from IGS analysis centers. In Equation (2), $\widetilde{dt}_r$ represents the receiver clock error after absorbing IF combination of the receiver hardware code bias on the first two frequencies. It is noted that the ambiguity associated with the IF combination cannot be directly expressed in the form $\lambda_{IF} N_{IF}$ where N_{IF} is an integer. To resolve the ambiguity parameters, N_{IF} can be decomposed into a combination of the narrow-lane ambiguity $N^s_{1,r}$ and the wide-lane ambiguity $N^s_{WL,r}$. The wavelength of the narrow-lane ambiguity is approximately 11 cm for GPS L1/L2 and Galileo E1/E5a. Meanwhile, to facilitate ambiguity resolution, satellite-based single differencing is applied between the float ambiguities to eliminate receiver hardware phase biases, denoted as $\widetilde{B}_{12}$. $\epsilon_{P_{IF}}$ and $\epsilon_{L_{IF}}$ are the respective unmodeled error terms for pseudorange and carrier phase measurement after IF linear combination. The noise for both measurements is amplified by a factor of approximately 3 and 2.6 for GPS L1/L2 and Galileo E1/E5a, respectively. It is evident that the IF combinations are formulated respectively for code and phase measurements, indicating that the ionosphere delay is implicitly estimated without accounting for the fact that it is identical for both measurement types, even though pseudorange measurement is typically given much lower weights.

$$\begin{cases} P^s_{r,IF_{12}} & = \frac{f_1^2}{f_1^2-f_2^2}P_1 - \frac{f_2^2}{f_1^2-f_2^2}P_2 = \rho^s_r + c\widetilde{dt}_r + M^s_r T_r + \epsilon_{P_{IF}} \\ L^s_{r,IF_{12}} & = \frac{f_1^2}{f_1^2-f_2^2}L_1 - \frac{f_2^2}{f_1^2-f_2^2}L_2 = \rho^s_r + c\widetilde{dt}_r + M^s_r T_r + \lambda_{IF} N_{IF} + \widetilde{B}_{12} + \epsilon_{L_{IF}} \end{cases} \tag{2}$$

2.1.2. Triple-TCAR Model

Different methods have been investigated to form linear combinations with triple-frequency measurements [31]. In this study, the ionosphere-free combinations between frequency 1 and 2 and frequency 1 and 3 have been adopted to compute the float solution, shown in Equation (3). The measurement noise for the IF combination between GPS L1/L5 and Galileo E1/E5b is amplified by a factor of approximately 2.6 and 2.8, respectively. Same as Equation (2), $\widetilde{dt}_r$ in Equation (3) represents the receiver clock error containing the IF combination of receiver hardware code bias on frequency 1 and 2. Note that the bias term $\widetilde{b}_{dcb}$ in $P^s_{r,IF_{13}}$ is critical to absorb the differential code bias between two linear combinations of different frequency pairs. Meanwhile, $\widetilde{B}_{12}$ and $\widetilde{B}_{13}$ are added to the IF phase measurements to align with the receiver clock error derived from pseudorange measurements. For the ambiguity resolution, a triple-frequency carrier phase ambiguity resolution (TCAR) is conducted. The EWL ambiguities derived from HMW combinations between GPS L2/L5 and Galileo E5a/E5b are first resolved using the rounding method. The wavelength reaches up to 5.86 and 9.77 m for GPS and Galileo, respectively, enabling a near-instantaneous fixing of the EWL ambiguities [10,20]. This, in turn, accelerates the fixing of the WL ambiguities compared to the Dual-IF method in Section 2.1.1. The NL ambiguities are subsequently resolved.

$$\begin{cases} P^s_{r,IF_{12}} & = \frac{f_1^2}{f_1^2-f_2^2}P_1 - \frac{f_2^2}{f_1^2-f_2^2}P_2 = \rho^s_r + c\widetilde{dt}_r + M^s_r T_r + \epsilon_{P_{IF_{12}}} \\ P^s_{r,IF_{13}} & = \frac{f_1^2}{f_1^2-f_3^2}P_1 - \frac{f_3^2}{f_1^2-f_3^2}P_3 = \rho^s_r + c\widetilde{dt}_r + M^s_r T_r + \widetilde{b}_{dcb} + \epsilon_{P_{IF_{13}}} \\ L^s_{r,IF_{12}} & = \frac{f_1^2}{f_1^2-f_2^2}L_1 - \frac{f_2^2}{f_1^2-f_2^2}L_2 = \rho^s_r + c\widetilde{dt}_r + M^s_r T_r + \lambda_{IF_{12}} N_{IF_{12}} + \widetilde{B}_{12} + \epsilon_{L_{IF_{12}}} \\ L^s_{r,IF_{13}} & = \frac{f_1^2}{f_1^2-f_3^2}L_1 - \frac{f_3^2}{f_1^2-f_3^2}L_3 = \rho^s_r + c\widetilde{dt}_r + M^s_r T_r + \lambda_{IF_{13}} N_{IF_{13}} + \widetilde{B}_{13} + \epsilon_{L_{IF_{13}}} \end{cases} \tag{3}$$

It is important to consider the correlation between $P^s_{r,IF_{12}}$ and $P^s_{r,IF_{13}}$, as well as $L^s_{r,IF_{12}}$ and $L^s_{r,IF_{13}}$, when determining the stochastic model of the measurements in this model. The two combinations based on different frequency pairs are not completely independent since they both use the same measurement $P^s_{r,1}$ and $L^s_{r,1}$. Consequently, the corresponding measurement variance–covariance matrix is not diagonal. For the mixed processing of GPS satellites, the dual-frequency satellites are processed with Equation (2), and the satellites with triple-frequency measurements are processed with Equation (3).

2.1.3. Triple-Uncomb Model

The uncombined PPP model directly makes use of raw GNSS observables. It is notable that, in Equation (1), all the parameters cannot be estimated simultaneously due to the rank deficiency of the system. Hence, reparameterization is a key in the uncombined model [32]. Equation (4) presents a reparameterized formulation of the triple-frequency uncombined PPP model. Following the IGS convention, clock datum is defined by pseudorange measurements on L1 (C1W) and L2 (C2W) for GPS and E1 (C1C) and E5a (C5Q) for Galileo. The receiver hardware code biases on the first two frequencies are assimilated into the reparameterized receiver clock $\widetilde{dt}_r$ and ionospheric delays $\widetilde{I}^s_{r,1}$, while the receiver hardware bias $\widetilde{b}_{r,3}$ on the third frequency stays to absorb the between-frequency difference of code hardware biases, the so-called Inter-Frequency Bias (IFB). Inter-Frequency Clock Bias (IFCB), denoted as $\widetilde{B}_{r,3}$, is introduced into the phase measurement on the third frequency to address the inconsistency in the clock corrections estimated from the L1/L2 and L1/L5 combinations [33,34]. To ensure a mathematically rigorous formulation, $\widetilde{B}_{r,1}$ and $\widetilde{B}_{r,2}$ are introduced to account for receiver phase biases, thereby aligning with the receiver pseudorange clock. The biases are within half a wavelength. In practice, PPP users apply OSB products directly to raw observables to correct for the hardware biases on the satellite side. Again, single difference is applied between the uncombined float ambiguities to keep their integer nature, enabling ambiguity resolution. For GPS satellites transmitting only dual-frequency measurements, the same model with only $P^s_{r,1}, P^s_{r,2}, L^s_{r,1}, L^s_{r,2}$ measurements is used.

$$\begin{cases} P^s_{r,1} & = \rho^s_r + c\widetilde{dt}_r + \gamma_1 \widetilde{I}^s_{r,1} + M^s_r T_r - b^s_1 + \epsilon_{P_1} \\ P^s_{r,2} & = \rho^s_r + c\widetilde{dt}_r + \gamma_2 \widetilde{I}^s_{r,1} + M^s_r T_r - b^s_2 + \epsilon_{P_2} \\ P^s_{r,3} & = \rho^s_r + c\widetilde{dt}_r + \gamma_3 \widetilde{I}^s_{r,1} + M^s_r T_r + \widetilde{b}_{r,3} - b^s_3 + \epsilon_{P_3} \\ L^s_{r,1} & = \rho^s_r + c\widetilde{dt}_r - \gamma_1 \widetilde{I}^s_{r,1} + M^s_r T_r + \lambda_1 (\widetilde{N}^s_{r,1} + \widetilde{B}_{r,1} - B^s_1) + \epsilon_{L_1} \\ L^s_{r,2} & = \rho^s_r + c\widetilde{dt}_r - \gamma_2 \widetilde{I}^s_{r,1} + M^s_r T_r + \lambda_2 (\widetilde{N}^s_{r,2} + \widetilde{B}_{r,2} - B^s_2) + \epsilon_{L_2} \\ L^s_{r,3} & = \rho^s_r + c\widetilde{dt}_r - \gamma_3 \widetilde{I}^s_{r,1} + M^s_r T_r + \lambda_3 (\widetilde{N}^s_{r,3} + \widetilde{B}_{r,3} - B^s_3) + \epsilon_{L_3} \end{cases} \tag{4}$$

2.2. PPP Models with Ambiguity Constraints

This subsection introduces the PPP models that incorporate two different types of ambiguity constraints into the triple-frequency uncombined PPP model.

2.2.1. Triple-Uncomb+N1&N2 Model

To fully leverage triple-frequency measurements and optimize performance, the triple-frequency uncombined model can incorporate the resolved ambiguities N1 and N2 from the Dual-IF model. This approach is referred to as the Triple-Uncomb+N1&N2 model in this study. Adding integer ambiguities on frequency 1 and 2 as pseudo-measurements, Equation (4) turns into Equation (5). As satellite-based single differences are applied to the float ambiguities for ambiguity resolution, the ambiguity constraints derived from the Dual-IF model are therefore the differenced integer ambiguities between satellite s and reference satellite ref, denoted as $\hat{N}^{s,ref}_{r,1}$ and $\hat{N}^{s,ref}_{r,2}$. δ_{N_1} and δ_{N_2} denote the integer offsets due to the potential incorrect fixing of the ambiguity constraints on frequency 1 and 2, respectively. Note $\delta_{N_1}, \delta_{N_2} \in \mathbb{Z}$.

$$\begin{cases} P^s_{r,1} & = \rho^s_r + c\widetilde{dt}_r + \gamma_1 \widetilde{I}^s_{r,1} + M^s_r T_r - b^s_1 + \epsilon_{P_1} \\ P^s_{r,2} & = \rho^s_r + c\widetilde{dt}_r + \gamma_2 \widetilde{I}^s_{r,1} + M^s_r T_r - b^s_2 + \epsilon_{P_2} \\ P^s_{r,3} & = \rho^s_r + c\widetilde{dt}_r + \gamma_3 \widetilde{I}^s_{r,1} + M^s_r T_r + \widetilde{b}_{r,3} - b^s_3 + \epsilon_{P_3} \\ L^s_{r,1} & = \rho^s_r + c\widetilde{dt}_r - \gamma_1 \widetilde{I}^s_{r,1} + M^s_r T_r + \lambda_1 (\widetilde{N}^s_{r,1} + \widetilde{B}_{r,1} - B^s_1) + \epsilon_{L_1} \\ L^s_{r,2} & = \rho^s_r + c\widetilde{dt}_r - \gamma_2 \widetilde{I}^s_{r,1} + M^s_r T_r + \lambda_2 (\widetilde{N}^s_{r,2} + \widetilde{B}_{r,2} - B^s_2) + \epsilon_{L_2} \\ L^s_{r,3} & = \rho^s_r + c\widetilde{dt}_r - \gamma_3 \widetilde{I}^s_{r,1} + M^s_r T_r + \lambda_3 (\widetilde{N}^s_{r,3} + \widetilde{B}_{r,3} - B^s_3) + \epsilon_{L_3} \\ \hat{N}^{s,ref}_{r,1} & = \widetilde{N}^s_{r,1} - \widetilde{N}^{ref}_{r,1} + \delta_{N_1} \\ \hat{N}^{s,ref}_{r,2} & = \widetilde{N}^s_{r,2} - \widetilde{N}^{ref}_{r,2} + \delta_{N_2} \end{cases} \tag{5}$$

In practice, this model is implemented with two Kalman filters running in parallel. First, the conventional IF PPP-AR model is applied using dual-frequency measurements to resolve ambiguities N1 and N2. Then, the triple-frequency uncombined model is employed with additional resolved ambiguity constraints to N1 and N2 from the first step. In such way, the high correlations between the parameters are largely reduced to better facilitate ambiguity resolution. Notably, this model increases computational complexity. The high computational cost of the Triple-Uncomb+N1&N2 model makes it less feasible for real-time applications, but it remains beneficial for post-processing, particularly for facilitating ambiguity resolution on the third frequency.

- Reference Satellite Change

A reference satellite is selected for each system (GPS/Galileo) such that the change of the reference satellite is minimized. Particularly for GPS, different reference satellites may be chosen in the two successive filters. In the second filter, where both dual- and triple-frequency satellites are processed, a triple-frequency satellite is selected as the reference satellite to establish the datum for all three frequencies. In contrast, a dual-frequency satellite may be used as the reference in the first filter, where only two frequencies are involved. This discrepancy, however, does not affect the results, as the ambiguity constraints N1 and N2 are mapped and re-differenced between the filters using a transformation matrix. The key is to correctly determine the transformation matrix based on the chosen reference satellite.

- Conditions to apply N1 and N2 constraints

Despite the advantages of adding ambiguity constraints, it is important to make sure the ambiguity constraints are correctly resolved as using incorrect ambiguities would despair the entire solution. To ensure the correctness of the ambiguity constraints, for a given epoch, they are only applied when more than half of the satellites have fixed ambiguities on frequencies 1 and 2. If this condition is not met, the constraints are not applied. Additionally, in principle, the N1 and N2 ambiguity constraints could be replaced with N1 and N3 ambiguities if dual-frequency PPP with frequency 1 and 3 were conducted first. However, since all GPS satellites currently transmit L1 and L2 signals, we opt to perform dual-frequency PPP on frequencies 1 and 2 in this study.

2.2.2. Triple-Uncomb+EWL&WL Model

As mentioned in Section 2.1.2, the EWL and WL ambiguities derived from HMW combination can be rapidly resolved in triple-frequency PPP processing. To exploit this advantage, the resolved EWL and WL ambiguities are incorporated into the observation equations, imposing constraints on the differences between the unknown ambiguity parameters. In Equation (6), $\hat{N}^{s,ref}_{r,EWL}$ and $\hat{N}^{s,ref}_{r,WL}$ denote the resolved differenced EWL ambiguities and WL ambiguities between satellite s and reference satellite ref. They are added as pseudo-measurements in the equation. $\delta_{N_{EWL}}$ and $\delta_{N_{WL}}$ denote the integer offsets resulting from the potential incorrect fixing of the EWL and WL ambiguity constraints, where $\delta_{N_{EWL}}, \delta_{N_{WL}} \in \mathbb{Z}$. This model is similar to TCAR, as the EWL and WL ambiguities are resolved subsequently. However, as opposed to Triple-TCAR model where EWL and WL ambiguities solely assist in resolving narrow-lane ambiguities, in this model, they contribute directly to the filtering process.

$$\begin{cases} P^s_{r,1} &= \rho^s_r + c\widetilde{dt}_r + \gamma_1 \widetilde{I}^s_{r,1} + M^s_r T_r - b^s_1 + \epsilon_{P_1} \\ P^s_{r,2} &= \rho^s_r + c\widetilde{dt}_r + \gamma_2 \widetilde{I}^s_{r,1} + M^s_r T_r - b^s_2 + \epsilon_{P_2} \\ P^s_{r,3} &= \rho^s_r + c\widetilde{dt}_r + \gamma_3 \widetilde{I}^s_{r,1} + M^s_r T_r + \widetilde{b}_{r,3} - b^s_3 + \epsilon_{P_3} \\ L^s_{r,1} &= \rho^s_r + c\widetilde{dt}_r - \gamma_1 \widetilde{I}^s_{r,1} + M^s_r T_r + \lambda_1 (\widetilde{N}^s_{r,1} + \widetilde{B}_{r,1} - B^s_1) + \epsilon_{L_1} \\ L^s_{r,2} &= \rho^s_r + c\widetilde{dt}_r - \gamma_2 \widetilde{I}^s_{r,1} + M^s_r T_r + \lambda_2 (\widetilde{N}^s_{r,2} + \widetilde{B}_{r,2} - B^s_2) + \epsilon_{L_2} \\ L^s_{r,3} &= \rho^s_r + c\widetilde{dt}_r - \gamma_3 \widetilde{I}^s_{r,1} + M^s_r T_r + \lambda_3 (\widetilde{N}^s_{r,3} + \widetilde{B}_{r,3} - B^s_3) + \epsilon_{L_3} \\ \hat{N}^{s,ref}_{r,EWL} &= (\widetilde{N}^s_{r,2} - \widetilde{N}^s_{r,3}) - (\widetilde{N}^{ref}_{r,2} - \widetilde{N}^{ref}_{r,3}) + \delta_{N_{EWL}} \\ \hat{N}^{s,ref}_{r,WL} &= (\widetilde{N}^s_{r,1} - \widetilde{N}^s_{r,2}) - (\widetilde{N}^{ref}_{r,1} - \widetilde{N}^{ref}_{r,2}) + \delta_{N_{WL}} \end{cases} \tag{6}$$

Practically, this model is implemented with a single filter, similar to the Triple-Uncomb model, although it involves additional calculations and resolutions for EWL and WL ambiguities. This model is well suited for real-time processing, as EWL ambiguities can be resolved almost instantaneously, and the rounding method does not impose a significant computational burden.

3. Data and Processing Strategy

To validate the proposed algorithms and compare the performance, 11 IGS stations have been used, and their datasets during 10 days from day 301 to 310 in 2023 were processed. The 24 h datasets were split into 4 h sessions, with a sampling rate of 30 s. Figure 1 shows the distribution of the IGS sites used in the processing. The selected IGS sites cover multiple types of receivers, including Septentrio PolaRx5, Septentrio PolaRx5TR, Trimble Alloy, Trimble NetR9, Javad delta-3, and Leica GR50. Measurements from GPS L1, L2, and L5, along with Galileo E1, E5a, and E5b, are processed in the experiments. The satellite orbit and clock errors, along with code and phase biases are corrected using WUM rapid products [35]. The Phase Center Offset (PCO) and Phase Center Variation (PCV) for the satellite and receiver are corrected using the corresponding ANTEX file, i.e., IGS20.atx. Solid earth tides [36], phase wind-up [37], relativistic effects [38], and Shapiro effects are corrected following the IERS conventions. The IGS weekly combined SINEX solution is taken as reference and compared against the algorithm performance.

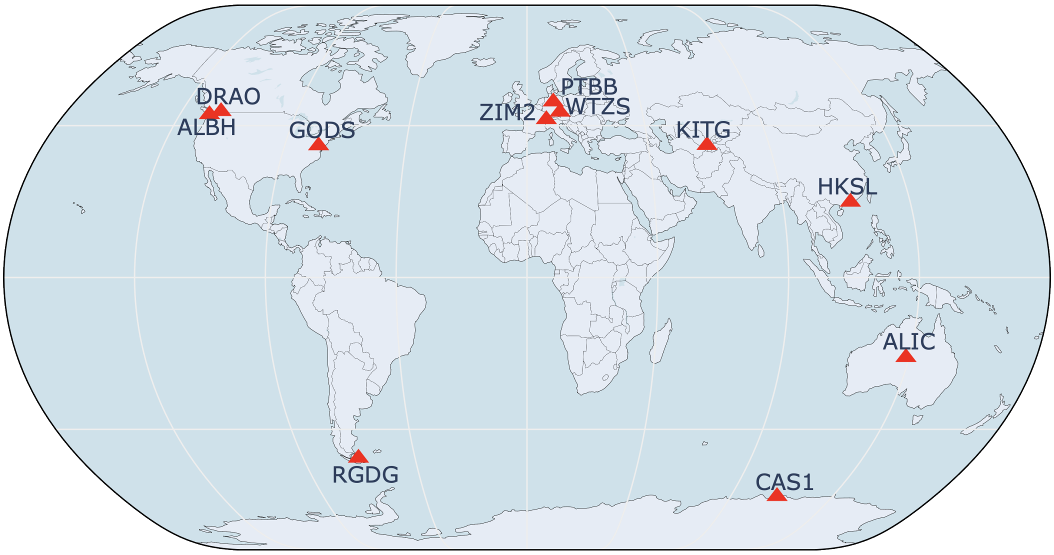

Figure 1. The distribution of the IGS sites used in the processing

The extended Kalman filter (EKF) was implemented across all five models for performance comparison. Table 2 shows the processing strategies in the EKF. The EKF parameters are initialized with least-square estimation for the first epoch. Note that in the uncombined model, ionospheric delays are estimated as white noise rather than random walk noise. The reason behind this is that, in the combined model where the ionospheric-free (IF) combination is used, it implicitly estimates the ionosphere as white noise. To ensure a fair comparison, we do not impose any constraints on the ionosphere. It is expected that adding a third frequency measurement, even when estimated as white noise, should outperform the Dual-IF model due to the inclusion of the additional frequency data.

Table 2. Processing strategies for the estimated parameters in extended Kalman filtering.

Parameters	Strategies
Signals	GPS L1/L2/L5[1], Galileo E1/E5a/E5b [1]
Elevation cutoff angle	7 °
Receiver coordinates	Static: estimated as constants
Receiver clock offsets	Estimated as white noise
Receiver hardware code bias	Estimated as time-constant term
Ionospheric delays [2]	Estimated as white noise

Table 2. *Cont.*

Parameters	Strategies
Tropospheric delays	VMF3 (Vienna Mapping Functions 3), residual zenith wet delay is estimated [5,39,40]
System time difference	Estimated with random walk process [41]
Ambiguities	Estimated as time-constant for each satellite arc
Weighting strategy	Elevation-dependent weighting: $\sigma = \frac{\sigma_{P/L}}{sin(ele)}$ with 0.3 and 0.002 m for code measurement σ_P and carrier phase measurement σ_L
Reference coordinates	IGS weekly combined SINEX solution

[1] L5 and E5b are only included in triple-frequency model processing, e.g., not in Dual-IF model; [2] Ionospheric delays are only estimated in the uncombined models.

Based on the float ambiguities estimated from EKF, mLAMBDA (modified Least-squares AMBiguity Decorrelation Adjustment) was applied to search for the optimal integer candidates [42–44]. It is a modified version of LAMBDA [45,46] and is more computationally efficient compared to LAMBDA. A ratio test with an empirical threshold of 3 is adopted to validate the fixed ambiguity candidates. Partial ambiguity resolution is employed when not all ambiguities can be fixed. The float ambiguities are first ranked based on the elevation angles and, along with their variance–covariance matrix, fed into mLAMBDA. A fixed solution is updated and adopted only when the number of fixed satellites reaches at least four; otherwise, the float solution is used instead. In the combined model, EWL and WL ambiguities are resolved using rounding method, the NL ambiguities are then subsequently resolved with mLAMBDA. The final ambiguity-fixed solutions in the combined model only refer to the solutions with all EWL/WL/NL ambiguities resolved. On the other hand, in the uncombined model, all float ambiguities are processed with mLAMBDA, which is more computationally intensive due to the large number of float ambiguities, around three times that of the combined model. It should be noted that due to the high correlation between ambiguities on different frequencies of the same satellite, i.e., $N^s_{r,1}$, $N^s_{r,2}$, $N^s_{r,3}$ as a triplet, they should always be processed together to optimize the decorrelation step in mLAMBDA. Note the fixing is only attempted for satellites with an elevation angle higher than 15 °. The threshold condition for ambiguity resolution remains the same across all five models. While the numerical results may vary under different thresholds, the overall conclusion remains valid.

4. Results and Discussion

This section starts with an analysis of how the uncombined model benefits from two different types of ambiguity constraints. Following this, the two ambiguity-constrained models are compared with the classical models in terms of their initial positioning results within the first 20 min and their overall performance. The analysis includes evaluations of convergence time, positioning errors, and ambiguity fixing rates.

4.1. On the Ambiguity Constraints in the Uncombined Models

Before diving into the performance of the five models, it is important to first understand the impact of the two types of ambiguity constraints on the uncombined model. In this study, 0.8% and 1.2% of the experiments failed to converge within the first hour for the Triple-Uncomb+N1&N2 and Triple-Uncomb+EWL&WL models, respectively. These failures are attributed to the incorrect ambiguity constraints, specifically the N1&N2 and EWL&WL ambiguities. Figure 2 presents the position errors and formal uncertainty of the float solutions for the Triple-Uncomb, Triple-Uncomb+N1&N2, and Triple-Uncomb+EWL&WL models as a function of time during the first hour for an example experiment (GODS, DOY301, 0:00–4:00 h).

The performance of the ambiguity constraints is evaluated relative to the Triple-Uncomb model. In Figure 2b, a significant improvement is observed at approximately 7.5 min, where the accuracy improves from the decimeter level to the millimeter level.

This improvement occurs as the N1 and N2 ambiguity constraints begin to influence the solution. As previously stated, these ambiguity constraints are applied only when more than half of the fixable satellites are successfully resolved, as the correctness of the ambiguity constraints is crucial for directly influencing the float solutions and all other state parameters. In addition to the drastic accuracy improvement, the formal uncertainty of the solution, represented by the shaded area, is also greatly reduced. This uncertainty is at sub-millimeter level as a result of incorporating the ambiguity constraints of N1 and N2. Notably, before the 7.5-min mark, both the accuracy and uncertainty of Figure 2b are identical to those of Figure 2a.

Regarding the impact of adding EWL and WL ambiguities as constraints, as illustrated in Figure 2c, these constraints have a more immediate effect, particularly in the east component, due to their faster resolution compared to the N1 and N2 ambiguity constraints. Specifically, EWL ambiguities are resolved almost instantaneously, while WL ambiguities are resolved within approximately 1 to 3 min. A comparison between Figure 2a,c reveals that the primary impact is observed in the east component. The Triple-Uncomb+EWL&WL model shows a notable reduction in uncertainty compared to the Triple-Uncomb model, as the shaded areas are smaller, particularly in the first 10 min. Additionally, between 5 and 10 min, Figure 2a exhibits a fluctuation in the error curve in the east component, indicating a degradation in accuracy, which is less pronounced in Figure 2c, leading to a smoother float solution.

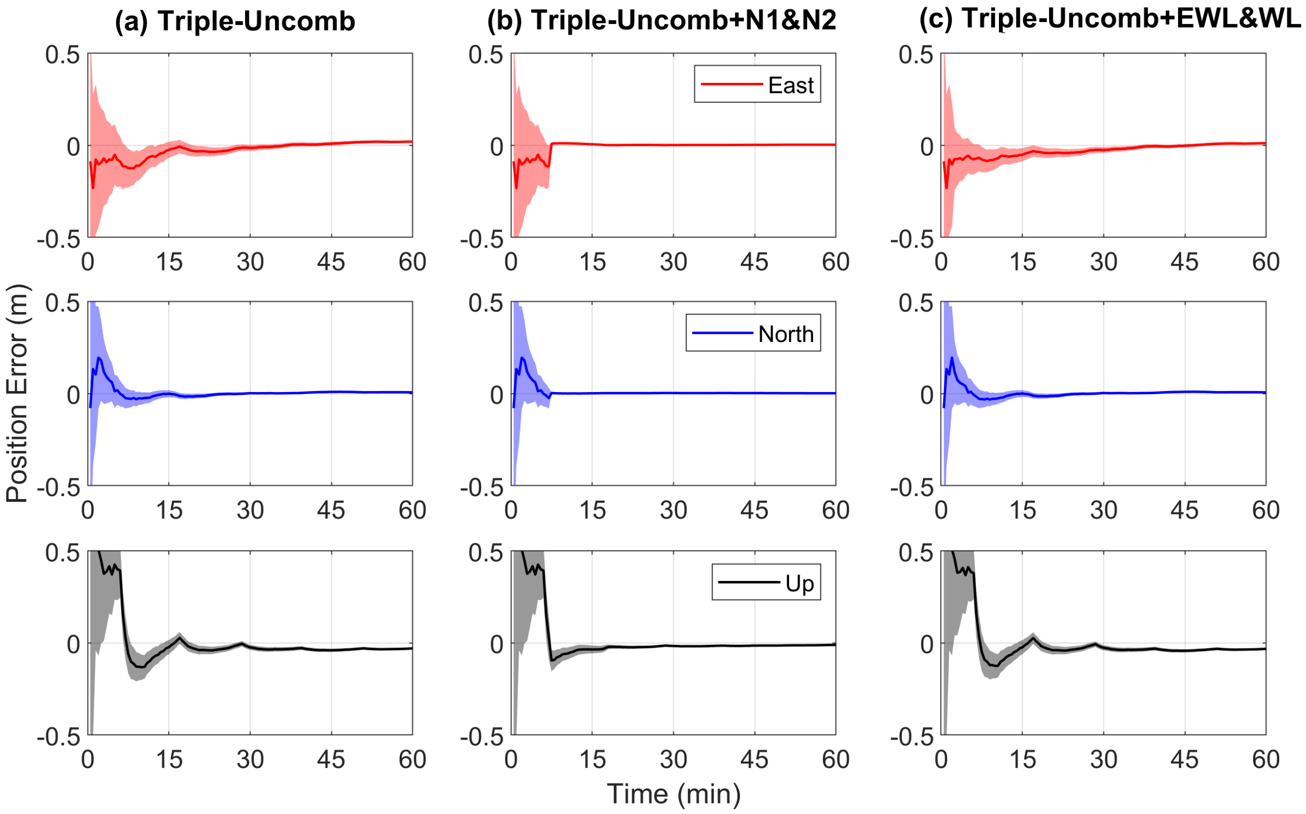

Figure 2. Float position errors and their formal uncertainty of the uncombined models in east (red), north (blue), and up (black) components during the first hour. The shaded area represents the error bar. (**a**) Triple-Uncomb model, (**b**) Triple-Uncomb+N1&N2 model, (**c**) Triple-Uncomb+EWL&WL model.

Figure 3 presents the histogram of the two types of ambiguity constraints affecting the solution. Figure 3a corresponds to the terms $\hat{N}_{r,1}^{s,ref}$ and $\hat{N}_{r,2}^{s,ref}$ in Equation (5). Figure 3b refers to the terms $\hat{N}_{r,EWL}^{s,ref}$ and $\hat{N}_{r,WL}^{s,ref}$ in Equation (6). The y-axis is displayed on a logarithmic scale, indicating that most constraints fall within 0.1 cycles. This is expected, as once the float solution converges, the constraints have minimal impact. The range of the N1 and N2 constraints is within approximately one cycle, while EWL and WL constraints fall within 0.1 and 0.3 cycles, respectively. Note that the different wavelengths result in different impacts on the solutions. Furthermore, Figure 3a displays the N1 and N2 constraints applied after 7.5 min, as this is when the required conditions are fulfilled. In contrast, Figure 3b shows the EWL and WL ambiguity constraints applied after 2 min.

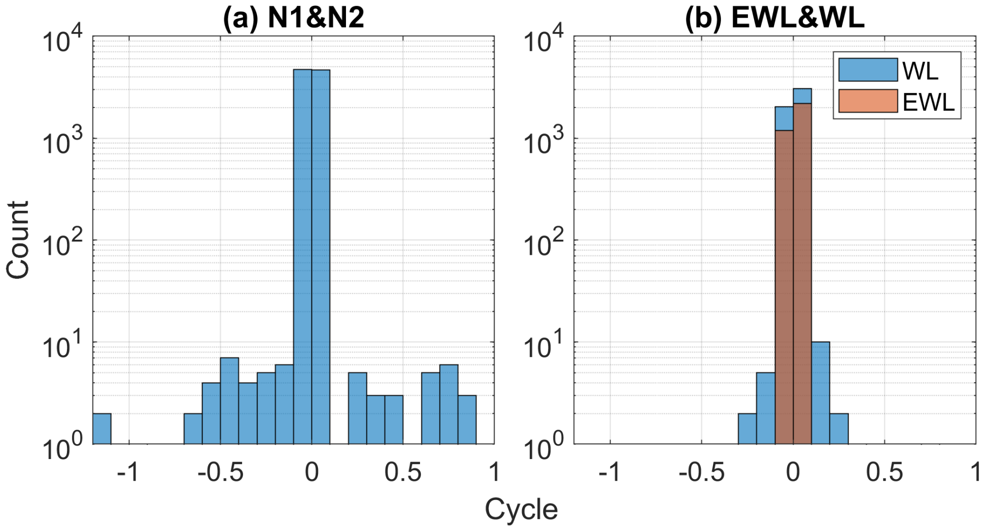

Figure 3. Histogram of the values of the ambiguity constraints in two models in experiment GODS, DOY 301, 0:00–4:00. (**a**) N1&N2 ambiguity constraints, (**b**) EWL&WL ambiguity constraints.

4.2. Initial Positioning Accuracy and Convergence

The initial positioning accuracy is assessed within the first 20 min. It is mainly influenced by measurement quality, the initial state parameter, and variance–covariance information for the filter if all other systematic errors are corrected. To ensure a fair comparison, identical input datasets, i.e., measurements after outlier screening, were used across all five models.

The estimated position errors for the east and north components within the first 20 min are illustrated in Figure 4. As it is difficult to obtain the true ambiguities in practice, a comparative approach is employed by analyzing the resolved ambiguity values across the five models. For N1 and N2 ambiguities, if at least three out of five models provide consistent values at the same epoch, the ambiguity is considered a validated fix; otherwise, it is classified as invalidated fix. For N3 ambiguity, with only four models involved, a validated fix requires consistent values from at least two models. In cases where the models are split two to two with different values, the fix is classified as invalidated. In Figure 4, three solution types—float, fixed, and validated fixed—are represented in different colors. The float solutions (in blue) appear to be quite consistent across the five models, with RMS error varying from 0.15 m to 0.18 m. The orange dots represent the fixed solutions where the ambiguities are successfully resolved in mLAMBDA and pass the ratio test. We can see that the green dots are subsets of the orange dots, representing the validated fixed solutions among all the fixed solutions. The green dots are scattered around the center, indicating smaller errors and suggesting they are correct fixes, with a horizontal RMS error of approximately 2 cm. The figure also shows that the two combined models exhibit more invalidated fixes compared to the three uncombined models.

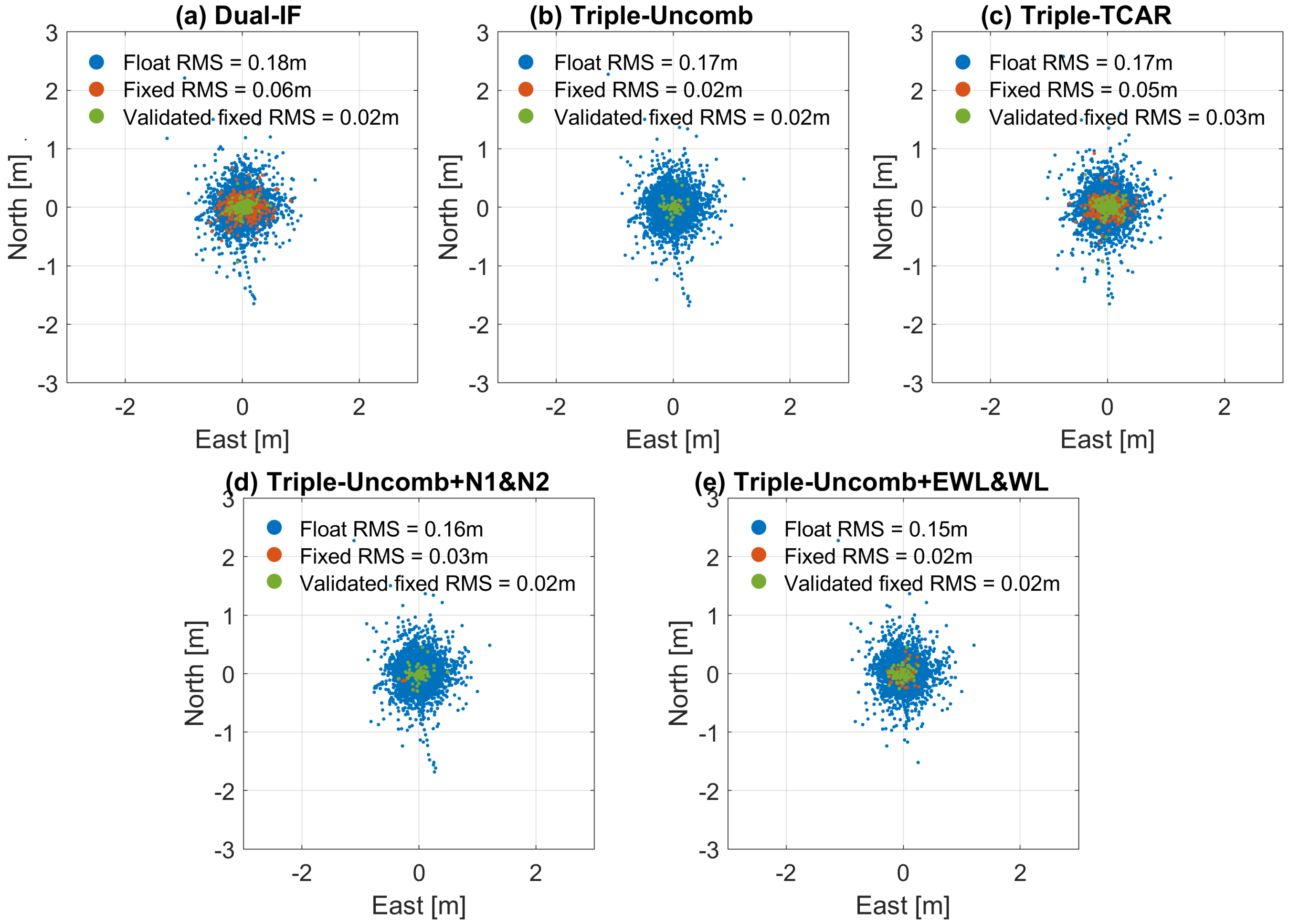

Figure 4. Horizontal scatter plot of position errors with RMS values during initial 20 min in all experiments. The blue, orange, and green dots represent float, fixed, and validated fixed solutions, respectively. (**a**) Dual-IF model, (**b**) Triple-Uncomb model, (**c**) Triple-TCAR model, (**d**) Triple-Uncomb+N1&N2 model, (**e**) Triple-Uncomb+EWL&WL model.

Table 3 presents the percentage of fixed solutions and validated fixed solutions relative to the total number of float solutions within the first 20 min. Among the five models, model (b) Triple-Uncomb has the lowest percentage of fixed solutions at around 58%; however, nearly all of these fixed solutions are validated. This is due to the high correlation among the large number of estimated state parameters in the uncombined model, which is particularly notable during the first few epochs when the EKF parameters are not yet converged. With ambiguity constraints incorporated, model (e) Triple-Uncomb+EWL&WL outperforms the other four models, achieving the highest percentages of both fixed and validated fixed solutions, at approximately 69% and 66%, respectively. Models (a), (c), and (e) exhibit approximately 3% of invalidated fixes. The common feature among these models is their use of the rounding method to resolve either EWL and WL, or only WL ambiguities, suggesting that rounding method may still result in a certain number of invalidated fixes. The use of mLAMBDA for WL ambiguity resolution might improve this. In contrast, models (b) and (d), which rely solely on mLAMBDA for ambiguity resolution, show less than 1% of invalidated fixes. Although both models have relatively lower percentage of fixed solutions, their fixes are more reliable. Additionally, the condition in model (d) where N1 and N2 ambiguity constraints are applied only when more than half of the satellite ambiguities are fixed may result in a lower fixing rate but ensure the reliability of the fixed solutions.

Table 3. Percentage of the fixed solution and validated fixed solution with respect to the float solution in the first 20 min. The values in the table are in percent. (**a**) Dual-IF model, (**b**) Triple-Uncomb model, (**c**) Triple-TCAR model, (**d**) Triple-Uncomb+N1&N2 model, (**e**) Triple-Uncomb+EWL&WL model.

	(a)	(b)	(c)	(d)	(e)
% of fixed solution	63.9	57.9	65.3	63.5	69.2
% of validated fixed solution	60.3	57.9	62.5	62.7	65.5

Figure 5 illustrates the cumulative distribution of the percentage of horizontally converged experiments for five models during the first 20 min, including both float and fixed solutions. In this study, convergence is defined when the horizontal or vertical error reaches 10 cm and remains within it for the next 10 min. We can see the blue dashed line (Dual-IF float) is at the lowest level compared to the other float solutions. This is expected, as the other models utilize triple-frequency measurements, which enhances the estimation of ionospheric delay. The red dashed line (Triple-Uncomb float) is slightly above the orange dashed line (Triple-TCAR float), particularly in the first 10 min. This discrepancy may be due to the fact that, although both models employ three frequency measurements and treat the ionosphere as white noise, the Triple-Uncomb model assumes a single common ionospheric estimate for all code and phase measurements, while the Triple-TCAR model does not, as it computes the IF combination individually using code and phase measurements from frequencies 1 and 2 and 1 and 3. Overall, the float solutions without ambiguity constraints are relatively similar. In contrast, the purple and green dashed lines are significantly higher than the other three float solutions. Notably, the purple dashed line (Triple-Uncomb+N1&N2 float) is comparable to the fixed solution, which is reasonable since this float solution incorporates the resolved N1 and N2 ambiguities, effectively making it a partially fixed solution. The green dashed line (Triple-Uncomb+EWL&WL float), although it only incorporates the relationships between ambiguities, clearly demonstrates its effectiveness in reducing uncertainty, accelerating convergence time, and facilitating ambiguity resolution. This impact is evident as the green solid line (Triple-Uncomb+EWL&WL fix) reaches the highest level, especially during the first 10 min.

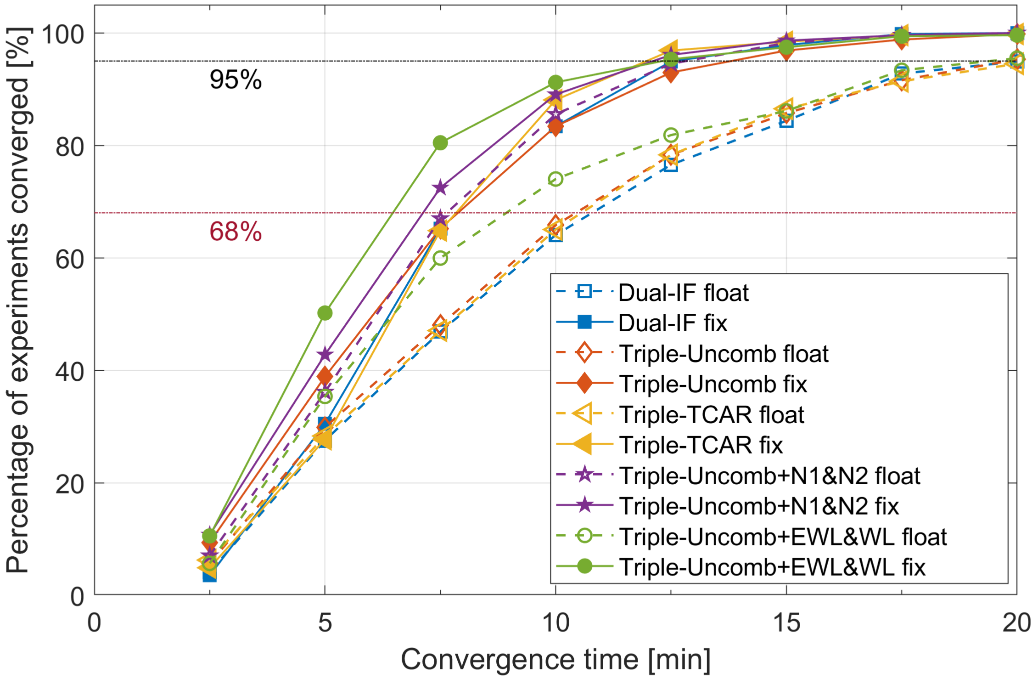

Figure 5. Cumulative distribution of the number of the converged experiments according to the horizontal convergence time. The black and red dotted lines denote the 95th and 68th percentile.

4.3. Overall Performance Analysis

To better analyze the overall positioning accuracy and its variation over time, in Figure 6 we present the epoch-by-epoch averaged horizontal and vertical errors along with their uncertainty derived from the scatter across all 555 experiments for the first hour. Sessions with missing observations or those that failed to converge within one hour are excluded. The horizontal blue line at 0.1 m marks the convergence threshold for both horizontal and vertical errors. In the float solutions for both horizontal and vertical components, as shown in Figure 6a,c, the purple dashed line (Triple-Uncomb+N1&N2 float) demonstrates the highest horizontal accuracy after approximately 6 min and consistently maintains the highest accuracy for the vertical component. Benefiting from the fixed ambiguity constraints N1 and N2, it achieves sub-centimeter horizontal accuracy by 15 min with minimal uncertainty. The models Dual-IF (blue dashed line), Triple-Uncomb (red dashed line), and Triple-TCAR (yellow dashed line) depict comparable float performance. However, within the initial 15 min, the Dual-IF model shows lower accuracy than the other models. Although the difference is small, this observation is still significant, as the same conclusion is drawn when results from different subsets of experiments are examined. Interestingly, the green dashed line (Triple-Uncomb+EWL&WL float) converges more rapidly than the purple dashed line during the first 6 min in the horizontal component, though this is not shown in the vertical component. The faster initial convergence facilitates ambiguity resolution, which may explain why the green solid lines in Figure 6b,d reach fixed solutions faster than the purple solid lines.

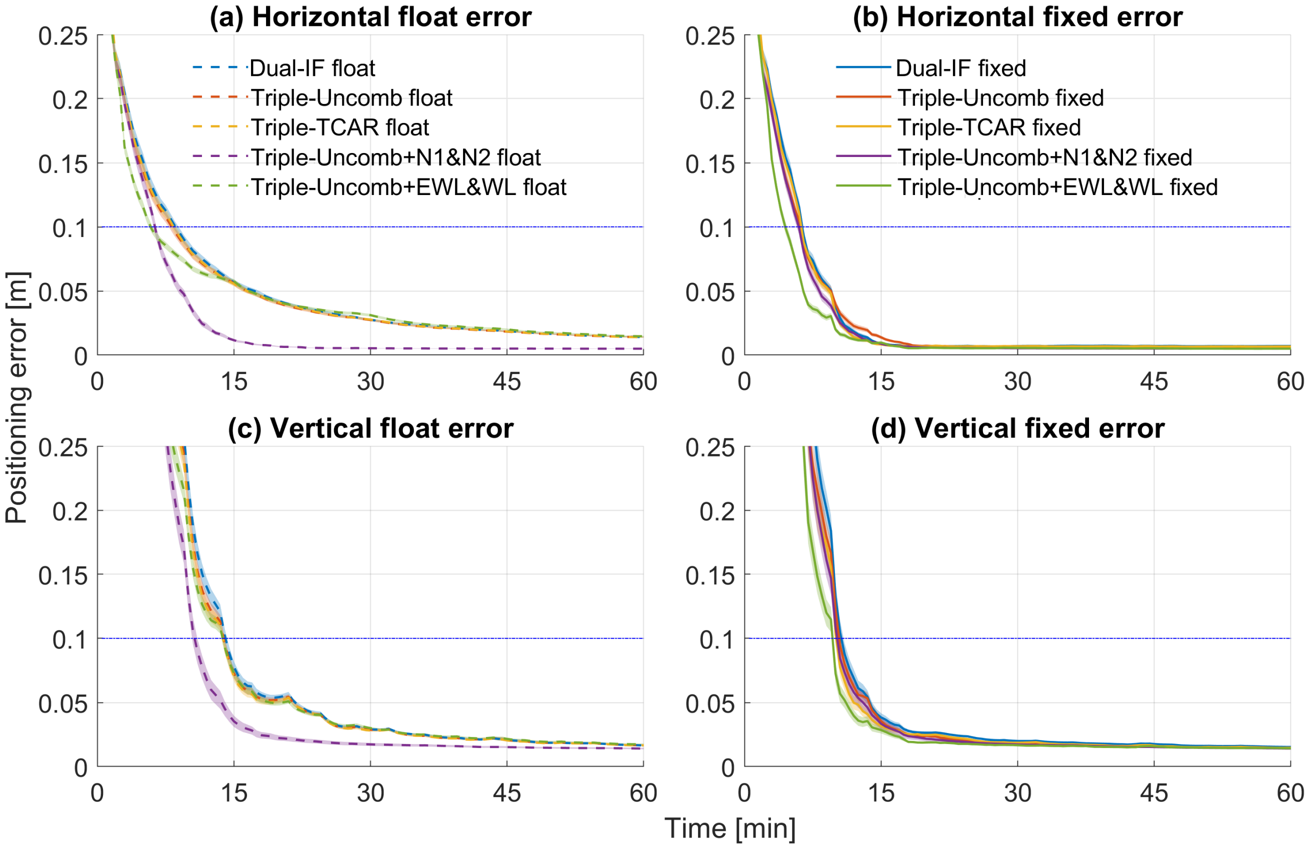

Figure 6. Averaged positioning error over time in horizontal and vertical components during the first hour. Blue, red, yellow, purple, and green lines represent Dual-IF, Triple-Uncomb, Triple-TCAR, Triple-Uncomb+N1&N2, and Triple-Uncomb+EWL&WL models, respectively. Shaded area represents the uncertainty of the solution. Blue horizontal line denotes the convergence level. (**a**) Horizontal float positioning error, (**b**) horizontal fixed positioning error, (**c**) vertical float positioning error, (**d**) vertical fixed positioning error.

A corresponding illustration of the convergence time for the five models in both horizontal and vertical components is shown in Figure 7. The convergence time is determined based on Figure 6, specifically identified as the points where the error curves intersect the 10 cm threshold. It is evident that the fixed solutions across all five models significantly reduce the convergence time, as expected. The Dual-IF model exhibits the longest convergence time, requiring 8.7 min horizontally and 14.1 min vertically for the float solution and 6.4 min horizontally and 10.7 min vertically for the fixed solution, with uncertainties of approximately 15 s for the float and 10 s for the fixed solutions, as indicated in the shaded area in Figure 6. Compared to the Triple-Uncomb model, the Triple-Uncomb+N1&N2 model reduces convergence time in the float solution from 8.2 to 6.4 min horizontally and from 13.9 to 10.7 min vertically, yielding improvements of 22% and 23%, respectively. It should be noted that since the ambiguity constraints N1 and N2 are derived from the Dual-IF model, the convergence of this model in practice is governed by the ambiguity fixing efficiency of the Dual-IF model and the convergence of the Triple-Uncomb model. Nonetheless, it is still interesting to see that if N1 and N2 are known a priori, convergence can be accelerated. The Triple-Uncomb+EWL&WL model reduces the horizontal convergence time to 5.9 min in the float solution, a 28% improvement, but has no obvious impact in the vertical component. This suggests that the EWL and WL ambiguity constraints enhance the horizontal positioning performance, specifically the east component, since fixing ambiguities is known to primarily improve accuracy in the east component as established in previous studies [14,47]. In the fixed solution, this model shortens convergence time by 1.6 min horizontally and 0.8 min vertically compared with the Triple-Uncomb model, corresponding to improvements of 26% and 8%. Overall, the fixed solution of the Triple-Uncomb+EWL&WL model achieves the fastest convergence, reaching 4.6 min horizontally and 9.7 min vertically.

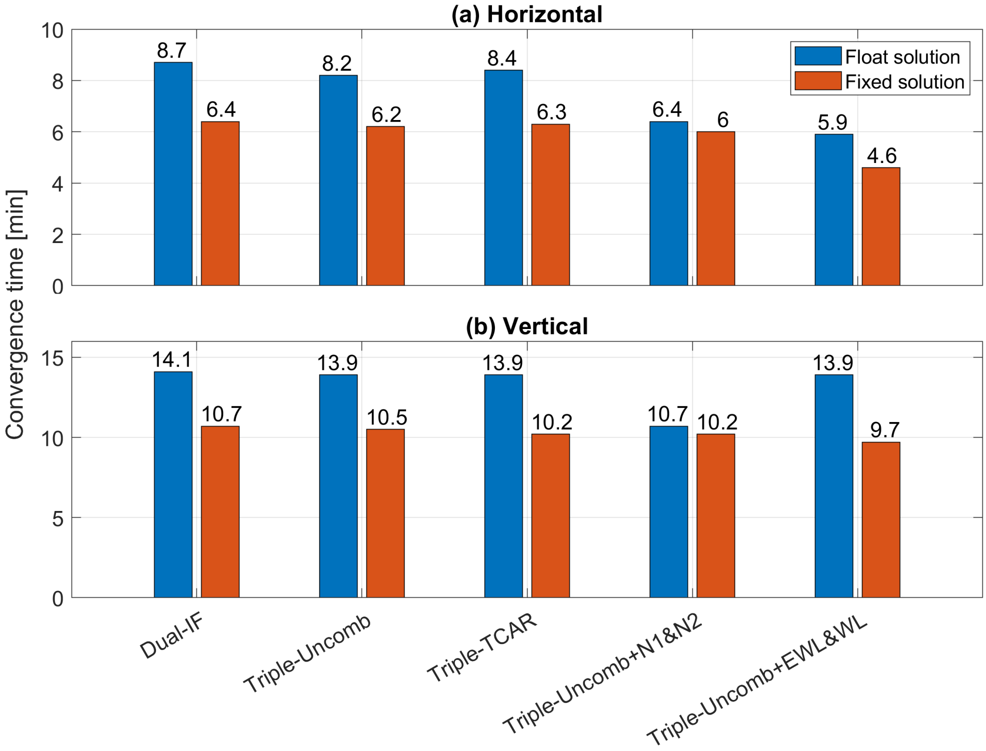

Figure 7. The averaged convergence time for float and fixed solution among five models. Convergence time statistics align with the results in Figure 6. (**a**) Horizontal component. (**b**) Vertical component.

To evaluate the final accuracy levels achieved by the solutions, Table 4 presents the averaged RMS position errors for all five models over the last three hours. For the float solutions, all four models—Dual-IF, Triple-Uncomb, Triple-TCAR, and Triple-

Uncomb+EWL&WL—converge to the same accuracy level, with 2D errors of 0.9 cm, up errors of 1.4 cm, and 3D errors of 1.7 cm. The float solution for the Triple-Uncomb+N1&N2 model, as being partially fixed, achieves better accuracy with errors of approximately 0.5 cm, 1.2 cm, and 1.3 cm for 2D, up, and 3D, respectively. Notably, for this model, the float and fixed solutions are identical. Among the fixed solutions, though all models perform closely, the two models with added ambiguity constraints exhibit slightly higher accuracy than the other three models.

Table 4. Average RMS position error for five models in the last three hours.

Model	**Average RMS Position Error (cm)**					
	Float			**Fix**		
	2D	**Up**	**3D**	**2D**	**Up**	**3D**
Dual-IF	0.9	1.4	1.7	0.7	1.4	1.6
Triple-Uncomb	0.9	1.4	1.7	0.6	1.3	1.5
Triple-TCAR	0.9	1.4	1.7	0.7	1.3	1.6
Triple-Uncomb+N1&N2	0.5	1.2	1.3	0.5	1.2	1.3
Triple-Uncomb+EWL&WL	0.9	1.4	1.7	0.5	1.2	1.4

Figure 8 presents the averaged fixing rate and validated fixing rate across all experiments in a 4 h period. The fixing rate, shown in orange, represents the ratio of resolved ambiguities to the total number of ambiguities targeted for fixing over the 4 h time period. The validated fixing rate, shown in green, is determined the same way as explained in Section 4.2. In this figure, the Dual-IF model demonstrates a fixing rate of approximately 88%, with a validated fixing rate of 86%. The Triple-Uncomb model shows a fixing rate and validated fixing rate both around 80%. This coincides with the previous observation during the first 20 min. It should be noted that the fixing rate is likely to improve if an external dynamic model for the ionosphere is applied, rather than estimating it as white noise. The Triple-TCAR model performs better compared to the Dual-IF model, achieving a fixing rate of 90% and a validated fixing rate of approximately 88%, indicating the advantage of incorporating the third frequency measurement. Clearly, the Triple-Uncomb+N1&N2 model achieves the highest fixing rate of 90% and a validated fixing rate of around 89%. This highlights the effectiveness of incorporating N1 and N2 ambiguity constraints, which enhances the ambiguity fixing and its reliability. While earlier analysis, shown in Table 3, indicates that the Triple-Uncomb+EWL&WL model exhibits a higher fixing rate and validated fixing rate within the initial 20 min, the Triple-Uncomb+N1&N2 model appears to surpass it over the longer term. This further demonstrates that this model is particularly well-suited for post-processing applications, where convergence time and computational load are not critical performance metrics, but reliable ambiguity resolution, high fixing rate, and enhanced accuracy are of greater importance. The Triple-Uncomb+EWL&WL model also demonstrates strong performance, with a fixing rate of approximately 90% and a validated fixing rate of 89%. The inclusion of EWL and WL constraints in the uncombined float solution improves the probability of the correct fix. This is particularly evident when we compare it with Triple-TCAR model. Despite the similar fixing rates between the two models, the Triple-Uncomb+EWL&WL model achieves a higher validated fixing rate than the Triple-TCAR model.

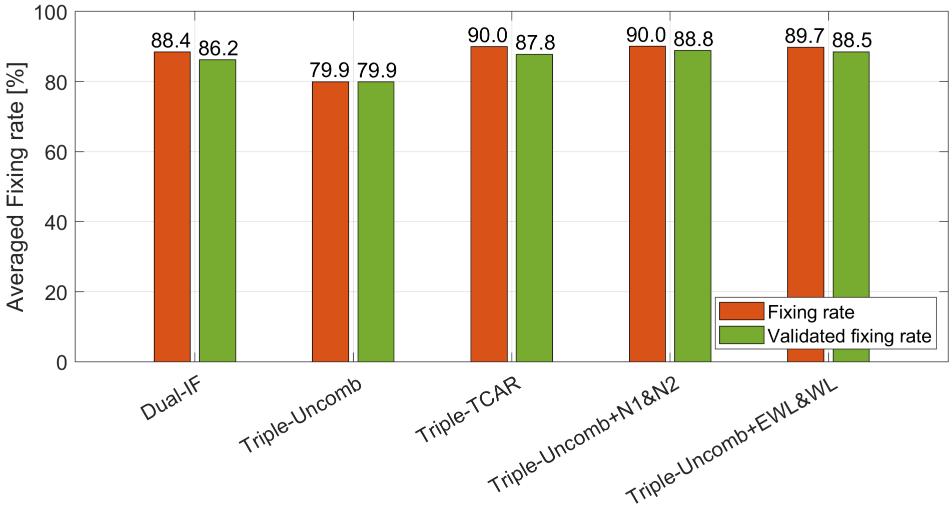

Figure 8. Averaged fixing rate and validated fixing rate for five models for all experiments. The fixing rate and validated fixing rate are both averaged over all experiments.

5. Conclusions

In this work, two approaches for integrating ambiguity constraints, i.e., N1&N2 ambiguities and EWL&WL ambiguities, into the triple-frequency uncombined PPP model are introduced and evaluated. The results demonstrate that incorporating ambiguity constraints effectively improve the PPP positioning performance, including accuracy, convergence time, and ambiguity resolution. The impact of N1&N2 constraints on the solution takes slightly longer, a few minutes, whereas the EWL&WL constraints begin to influence the solution within the first 2 min. Compared to the uncombined PPP-AR model without any constraints, integrating N1&N2 constraints as a priori notably accelerates the convergence of the float solution, reducing horizontal convergence time from 8.2 min to 6.4 min and vertical convergence time from 13.9 min to 10.7 min. On the other hand, integrating EWL&WL constraints reduces the horizontal convergence time from 8.2 to 5.9 min in the float solution, an improvement of around 28%, with no notable vertical enhancement. In fixed solutions, EWL&WL constraints result in improvements of approximately 26% and 8% for horizontal and vertical convergence, respectively. Overall, both approaches enhance the performance of the uncombined triple-frequency PPP model, with the average validated fixing rate reaching up to 89%.

One of the key challenges in integrating N1&N2 ambiguities is to determine the appropriate conditions under which the N1 and N2 ambiguities should be applied. It is crucial to verify the correctness of these fixed ambiguities to fully harness their benefits; otherwise, incorrect fixes can lead to degraded positioning solutions. In this study, we established a condition that N1 and N2 ambiguities are applied as constraints only when at least half of the satellites have been successfully fixed. Further investigation in this area is necessary to explore potential performance enhancements. Additionally, future work should also consider expanding the models to encompass multi-frequency measurements.

Meanwhile, the PPP users have to be mindful of the trade-off between the computational efficiency and the gain in positioning performance. While incorporating N1 &N2 constraints enhances ambiguity resolution efficiency, it requires two filters in practice. This makes it less feasible for real-time applications, although it remains effective for post-processing scenarios. In contrast, employing EWL and WL ambiguity constraints requires only a single filter, enabling rapid convergence and making this approach well suited for real-time processing. Therefore, it is essential for users to select the model that best aligns with the specific requirements of their application.

Author Contributions: Conceptualization, Y.L., U.H., and B.D.; methodology, Y.L.; software, Y.L.; investigation, Y.L., U.H., and B.D.; writing—original draft preparation, Y.L.; writing—review and

editing, Y.L., U.H., and B.D.; visualization, Y.L.; supervision, U.H. and B.D. All authors have read and agreed to the published version of the manuscript.

Funding: This research received no external funding.

Data Availability Statement: GNSS observation data are publicly available from International GNSS Service (IGS). Satellite products used in this study are provided by WUM. All the data and products are publicly available through the respective websites.

Conflicts of Interest: Author Yichen Liu was employed by Bosch Research during the time this research was conducted. The remaining authors declare that the research was carried out without any commercial or financial relationships that could be construed as a potential conflict of interest.

References

1. Zumberge, J.F.; Heflin, M.B.; Jefferson, D.C.; Watkins, M.M.; Webb, F.H. Precise point positioning for the efficient and robust analysis of GPS data from large networks. *J. Geophys. Res. Solid Earth* **1997**, *102*, 5005–5017. [CrossRef]
2. Kouba, J.; Héroux, P. Precise Point Positioning Using IGS Orbit and Clock Products. *GPS Solut.* **2001**, *5*, 12–28. [CrossRef]
3. Naciri, N.; Bisnath, S. Approaching global instantaneous precise positioning with the dual-and triple-frequency multi-GNSS decoupled clock model. *Remote Sens.* **2021**, *13*, 3768. [CrossRef]
4. Geng, J.; Guo, J.; Meng, X.; Gao, K. Speeding up PPP ambiguity resolution using triple-frequency GPS/BeiDou/Galileo/QZSS data. *J. Geod.* **2020**, *94*, 6. [CrossRef]
5. Glaner, M.F. Towards Instantaneous PPP Convergence Using Multiple GNSS Signals. Ph.D. Thesis, Technische Universität Wien, Vienna, Austria, 2022. . [CrossRef]
6. Brack, A.; Männel, B.; Schuh, H. Two-epoch centimeter-level PPP-RTK without external atmospheric corrections using best integer-equivariant estimation. *GPS Solut.* **2022**, *27*, 12. [CrossRef]
7. Tao, J.; Chen, G.; Guo, J.; Zhang, Q.; Liu, S.; Zhao, Q. Toward BDS/Galileo/GPS/QZSS triple-frequency PPP instantaneous integer ambiguity resolutions without atmosphere corrections. *GPS Solut.* **2022**, *26*, 127. [CrossRef]
8. Strasser, S.; Mayer-Gürr, T.; Zehentner, N. Processing of GNSS constellations and ground station networks using the raw observation approach. *J. Geod.* **2019**, *93*, 1045–1057. [CrossRef]
9. Zhang, B.; Hou, P.; Zha, J.; Liu, T. PPP–RTK functional models formulated with undifferenced and uncombined GNSS observations. *Satell. Navig.* **2022**, *3*, 3. [CrossRef]
10. Liu, G.; Zhang, X.; Li, P. Improving the performance of Galileo uncombined precise point positioning ambiguity resolution using triple-frequency observations. *Remote Sens.* **2019**, *11*, 341. [CrossRef]
11. Liu, Y.; Mikhaylov, N.; Hugentobler, U.; Duan, B. Triple-frequency PPP-AR model comparison from the user perspective: combined and uncombined models. In Proceedings of the IEEE/ION Position, Location and Navigation Symposium, PLANS, Monterey, CA, USA , 24–27 April 2023; pp. 867–874. [CrossRef]
12. Aggrey, J.; Bisnath, S. Improving GNSS PPP convergence: The case of atmospheric-constrained, multi-GNSS PPP-AR. *Sensors* **2019**, *19*, 587. [CrossRef] [PubMed]
13. Zhang, H.; Gao, Z.; Ge, M.; Niu, X.; Huang, L.; Tu, R.; Li, X. On the convergence of ionospheric constrained precise point positioning (IC-PPP) based on undifferential uncombined raw GNSS observations. *Sensors* **2013**, *13*, 15708–15725. [CrossRef] [PubMed]
14. Ge, M.; Gendt, G.; Rothacher, M.; Changhong, S.; Liu, J. Resolution of GPS Carrier-Phase Ambiguities in Precise Point Positioning (PPP) with Daily Observations. *J. Geod.* **2008**, *82*, 389–399. [CrossRef]
15. Laurichesse, D.; Mercier, F.; Berthias, J.P.; Broca, P.; Cerri, L. Integer ambiguity resolution on undifferenced GPS phase measurements and its application to PPP and satellite precise orbit determination. *Navig. J. Inst. Navig.* **2009**, *56*, 135–149. [CrossRef]
16. Collins, P. Isolating and estimating undifferenced GPS integer ambiguities. In Proceedings of the Institute of Navigation, National Technical Meeting. San Diego, CA, USA, 28–30 January 2008; Volume 2, pp. 720–732
17. Banville, S.; Geng, J.; Loyer, S.; Schaer, S.; Springer, T.; Strasser, S. On the interoperability of IGS products for precise point positioning with ambiguity resolution. *J. Geod.* **2020**, *94*, 10. [CrossRef]
18. Hatch, R.; Jung, J.; Enge, P.; Pervan, B. Civilian GPS: The Benefits of Three Frequencies. *GPS Solut.* **2000**, *3*, 1–9. [CrossRef]
19. Vollath, U.; Birnbach, S.; Landau, L.; Fraile-Ordoñez, J.M.; Martí-Neira, M. Analysis of Three-Carrier Ambiguity Resolution Technique for Precise Relative Positioning in GNSS-2. *Navigation* **1999**, *46*, 13–23. [CrossRef]
20. Geng, J.; Bock, Y. Triple-frequency GPS precise point positioning with rapid ambiguity resolution. *J. Geod.* **2013**, *87*, 449–460. [CrossRef]
21. Zhao, Q.; Dai, Z.; Hu, Z.; Sun, B.; Shi, C.; Liu, J. Three-carrier ambiguity resolution using the modified TCAR method. *GPS Solut.* **2015**, *19*, 589–599. [CrossRef]
22. Li, T.; Wang, J.; Laurichesse, D. Modeling and quality control for reliable precise point positioning integer ambiguity resolution with GNSS modernization. *GPS Solut.* **2014**, *18*, 429–442. [CrossRef]

23. Schaer, S.; Villiger, A.; Arnold, D.; Dach, R.; Jäggi, A.; Prange, L. New ambiguity-fixed IGS clock analysis products at CODE. In Proceedings of the International GNSS Service Workshop, Wuhan, China, 29 October–2 November 2018.
24. Villiger, A.; Schaer, S.; Dach, R.; Prange, L.; Susnik, A.; Jäggi, A. Determination of GNSS pseudo-absolute code biases and their long-term combination. *J. Geod.* **2019**, *93*, 1487–1500. [CrossRef]
25. Liu, G.; Guo, F.; Wang, J.; Du, M.; Qu, L. Triple-frequency GPS un-differenced and uncombined PPP ambiguity resolution using observable-specific satellite signal biases. *Remote Sens.* **2020**, *12*, 2310. [CrossRef]
26. Li, B.; Mi, J.; Zhu, H.; Gu, S.; Xu, Y.; Wang, H.; Yang, L.; Chen, Y.; Pang, Y. BDS-3/GPS/Galileo OSB Estimation and PPP-AR Positioning Analysis of Different Positioning Models. *Remote Sens.* **2022**, *14*, 4207. [CrossRef]
27. Duan, B.; Hugentobler, U.; Montenbruck, O.; Steigenberger, P. Performance of Galileo satellite products determined from multi-frequency measurements. *J. Geod.* **2023**, *97*, 32. [CrossRef]
28. Hatch, R. The synergism of GPS code and carrier measurements. In Proceedings of the International Geodetic Symposium on Satellite Doppler Positioning, Las Cruces, NM, USA, 8–12 February 1982; pp. 1213–1231.
29. Melbourne, W. The case for ranging in GPS-based geodetic systems. In Proceedings of the 1st International Symposium on Precise Positioning with the Global Positioning System, Rockville, MD, USA, 15–19 April 1985; pp. 403–412.
30. Wübbena, G. Software Developments for Geodetic Positioning with GPS Using TI 4100 Code and Carrier Measurements. In Proceedings of the 1st International Symposium on Precise Positioning with the Global Positioning System, Rockville, MD, USA, 15–19 April 1985; pp. 373–386.
31. Guo, F.; Zhang, X.; Wang, J.; Ren, X. Modeling and assessment of triple-frequency BDS precise point positioning. *J. Geod.* **2016**, *90*, 1223–1235. [CrossRef]
32. Liu, Y.; Hugentobler, U.; Duan, B.; Mikhaylov, N.; Simon, J. Receiver Bias Estimation Strategy in the Uncombined Triple-Frequency PPP-AR Model. In Proceedings of the 36th International Technical Meeting of the Satellite Division of The Institute of Navigation (ION GNSS+), Denver, CO, USA, 11–15 September 2023; pp. 2570–2580. [CrossRef]
33. Duan, B.; Hugentobler, U.; Selmke, I.; Wang, N. Estimating ambiguity fixed satellite orbit, integer clock and daily bias products for GPS L1/L2, L1/L5 and Galileo E1/E5a, E1/E5b signals. *J. Geod.* **2021**, *95*, 44. [CrossRef]
34. Montenbruck, O.; Hugentobler, U.; Dach, R.; Steigenberger, P.; Hauschild, A. Apparent clock variations of the Block IIF-1 (SVN62) GPS satellite. *GPS Solut.* **2012**, *16*, 303–313. [CrossRef]
35. Geng, J.; Zhang, Q.; Li, G.; Liu, J.; Liu, D. Observable-specific phase biases of Wuhan multi-GNSS experiment analysis center's rapid satellite products. *Satell. Navig.* **2022**, *3*, 23. [CrossRef]
36. Petit, G.; Luzum, B. IERS conventions. 2010. Verlag des Bundesamts fur Kartographie und Geodasie, Frankfurt am Main. Available online: https://www.iers.org/SharedDocs/Publikationen/EN/IERS/Publications/tn/TechnNote36/tn36.pdf (accessed on 23 November 2024).
37. Wu, J.T.; Wu, S.C.; Hajj, G.; Bertiger, W.; Lichten, S.M. Effects of antenna orientation on GPS carrier phase. *Manuscr. Geod.* **1993**, *18*, 91–98. . [CrossRef]
38. Kouba, J. A Guide to Using International GNSS Service (IGS) Products. IGS Website. 2015. Available online: https://files.igs.org/pub/resource/pubs/UsingIGSProductsVer21_cor.pdf (accessed on 23 November 2024).
39. Landskron, D.; Böhm, J. VMF3/GPT3: Refined discrete and empirical troposphere mapping functions. *J. Geod.* **2018**, *92*, 349–360. [CrossRef]
40. Glaner, M.F.; Weber, R. An open-source software package for Precise Point Positioning: raPPPid. *GPS Solut.* **2023**, *27*, 174. [CrossRef]
41. Bahadur, B.; Nohutcu, M. PPPH: A MATLAB-based software for multi-GNSS precise point positioning analysis. *GPS Solut.* **2018**, *22*, 113. [CrossRef]
42. Chang, X.W.; Yang, X.; Zhou, T. MLAMBDA: A modified LAMBDA method for integer ambiguity determination. In Proceedings of the 61st Annual Meeting of The Institute of Navigation Cambridge, MA, USA, 27–29 June 2005; pp. 1086–1097.
43. Chang, X.; Xie, X.; Ghassemi, T. MLAMBDA: MATLAB package for integer least squares ambiguity determination. May 2016. Available online: https://www.cs.mcgill.ca/~chang/software/MLAMBDA_User_Guide.pdf (accessed on 23 November 2024).
44. Borno, M.A.; Chang, X.W.; Xie, X.H. On 'decorrelation' in solving integer least-squares problems for ambiguity determination. *Surv. Rev.* **2014**, *46*, 37–49. [CrossRef]
45. Teunissen, P.J. Success probability of integer GPS ambiguity rounding and bootstrapping. *J. Geod.* **1998**, *72*, 606–612. [CrossRef]
46. Teunissen, P.J. The least-squares ambiguity decorrelation adjustment: A method for fast GPS integer ambiguity estimation. *J. Geod.* **1995**, *70*, 65–82. [CrossRef]
47. Kouba, J.; Lahaye, F.; Tétreault, P. Precise Point Positioning. In *Springer Handbook of Global Navigation Satellite Systems*; Teunissen, P.J., Montenbruck, O., Eds.; Springer Handbooks: Springer, Cham, 2017._25 [CrossRef]